OPEN ACCESS

Optimised Pulse-Fitting for Robust Time-Domain Impedance Analysis of Automotive Lithium-Ion Cells under Application-Specific Pulse Conditions

To cite this article: Rico Klink *et al* 2026 *J. Electrochem. Soc.* **173** 170509

Journal of The Electrochemical Society, 2026 **173** 170509

Optimised Pulse-Fitting for Robust Time-Domain Impedance Analysis of Automotive Lithium-Ion Cells under Application-Specific Pulse Conditions

Rico Klink,[1,2,z] René H. E. van Doorn,[1] and André Weber[2]

[1]*AUDI AG, NSU-Str. 1, Neckarsulm, 74172, Germany*
[2]*Institute for Applied Materials—Electrochemical Technologies (IAM-ET), Karlsruhe Institute of Technology (KIT), Karlsruhe, 76131, Germany*

A pulse-fitting methodology for time-domain analysis of lithium-ion battery impedance is presented and systematically extended to address automotive-relevant measurement constraints under controlled test conditions, including non-ideal current profiles, limited stabilization times, measurement noise, low sampling frequencies, and SOC-dependent OCV contributions. Since no universally applicable test pulse exists for large-format automotive lithium-ion cells, pulse-based diagnostics require evaluation methods that remain robust under application-specific excitation conditions. In this work, a pulse-fitting methodology for time-domain analysis of lithium-ion battery impedance is systematically extended. The approach models the voltage response to current pulses using a physically motivated RC network, enabling the extraction of diffusion-related time constants without relying on frequency-domain techniques. Key enhancements include numerical convolution for non-ideal current profiles, incorporation of a dynamic open-circuit voltage, Tikhonov regularisation, and weighting and scaling strategies to improve robustness against noise and low sampling frequencies. Furthermore, a quadratic programming solver is introduced to increase stability for ill-conditioned problems, and an extrapolation method is proposed to account for insufficient voltage stabilization times. The methodology is validated using both synthetic and experimental pulse data, demonstrating reliable access to low-frequency impedance characteristics. The results highlight the potential of the approach for advanced state estimation and model development.

[DOI: 10.1149/1945-7111/ae9990]

Manuscript submitted May 31, 2026; revised manuscript received July 23, 2026. Published September 2, 2026.

Supplementary material for this article is available online

Symbol	Description	Unit
t	Time	s
t_0	Start time of the current pulse	s
T_p	Pulse duration	s
Δt	Time step	s
$i\,(t)$	Time-dependent current signal	A
I_p	Pulse current amplitude	A
$\sigma\,(t)$	Heaviside step function	—
$u\,(t)$	Cell overpotential/resulting cell voltage	V
$u_n\,(t)$	Overpotential of the nth RC element	V
U_OCV	Open-circuit voltage	V
$U_\mathrm{OCV,dyn}$	Dynamic open-circuit voltage during SOC change	V
ΔU	Voltage change	V
ΔQ	Charge change	As
$C_{\Delta Int}$	Differential capacitance derived from pulse	F
R_0	Ohmic resistance	Ω
R_n	Resistance of the nth RC element	Ω
C_n	Capacitance of the nth RC element	F
$\tau_n = R_nC_n$	Time constant of the RC element	s
τ_min	Minimum detectable time constant	s
τ_max	Maximum considered time constant	s
f_s	Sampling frequency	Hz
M	Number of data points	—
N	Number of RC elements	—
A	Kernel matrix	—
B	System matrix including OCV term	—
u	Voltage vector	V
x	Solution vector (RC values + OCV value)	—
λ	Regularisation weight	—
W	Diagonal weighting matrix	—
s	Column scaling matrix	—
I_reg	Tikhonov regularisation matrix (2nd derivative)	—
H	Hessian matrix in quadratic programming	—
f	Gradient vector in quadratic programming	—
$u_\mathrm{model}\,(t)$	Modelled cell voltage	V
$u_\mathrm{mess}\,(t)$	Measured cell voltage	V

Abbreviations

Abbreviation	Meaning
SOC	State of Charge
SOH	State of Health
DRT	Distribution of Relaxation Times
EIS	Electrochemical Impedance Spectroscopy
CMC	Cell Management Controller
FFT	Fast Fourier Transform
MWT	Morlet Wavelet Transformation
PHEV	Plug-in Hybrid Electric Vehicle
QP	Quadratic Programming
DVA	Differential Voltage Analysis
ICA	Incremental Capacity Analysis

Unit	Description
s	Seconds
A	Ampere
V	Volt
Ω	Ohm
F	Farad
Hz	Hertz
Ah	Ampere-hours
mVh	Millivolt per hour
C (Coulomb)	Electric charge

[z] E-mail: rico.klink@audi.de; rico.klink@kit.edu

The impedance of an electrochemical cell provides a fundamental basis for determining its electrochemical state and for developing model-based approaches. The classical method for its determination, Electrochemical Impedance Spectroscopy (EIS), is particularly advantageous for high-and mid-frequency ranges (typically $f > 0.01$ Hz)[1a] As the stimulation is limited to a single frequency, a higher accuracy can be obtained. In case of low impedance samples, inductive artefacts at high frequencies usually limit the analysable frequency range. For automotive battery cells with impedance values in the mΩ-to μΩ-range the maximum frequency is commonly in the range of a few 100 Hz to some kHz. An overview regarding dominant system specific time constants and their accessibility via frequency-and time-domain measurements are shown in Fig. 1.

In case of lithium-ion batteries, diffusive low-frequency processes in the liquid electrolyte and the active material often dominate the electrochemical behavior and limit the battery performance. Their time constants in the range of a few seconds to many hours or even days require impedance measurements down to very low frequencies in the μHz range, which leads to unacceptably long measurement durations (on the order of several hours). Furthermore, at low frequencies, the criteria of time invariance, causality and linearity are difficult to fulfil due to shifts in the state of charge (SOC), the SOC-setting current, the SOC history, and the requisite rest periods to measurement.[2] Adjusting (lowering) the excitation signal of EIS to compensate for these factors leads to a degraded signal-to-noise ratio.

As a result, for the study of the diffusion characteristics, which are predominantly present at low till ultra-low frequencies, time-domain measurements are the preferred, as demonstrated by Klotz et al.[3] These changes in diffusion characteristics are reflected primarily in the overpotential profile. Both the magnitude of the overpotential relative to the open-circuit voltage (OCV) and the relaxation behavior define the time constants of the diffusion characteristic and the diffusion impedance. The voltage response of the overall cell is the sum of the overpotentials of individual cell components.

The behavior depends, among other factors, on:

- SOC,
- temperature,
- state of health (SOH),
- mechanical fixture conditions of large-scale prismatic or pouch cells.

A direct calculation of diffusion coefficients from pulse characteristics, bypassing intermediate impedance calculation, can be performed using the procedure described by Cabañero et al.[4] which is largely equivalent to the methodologies used by others.[5–7] In this method, a pulse is applied to the system, and specific voltage points are used to calculate diffusion coefficients of the tested setup (either full or half-cell level) directly.

In an alternative approach, the impedance behavior can be used for diffusion coefficient calculations. Different impedance calculation approaches are known. An overview is given by Klink et al.[8]

As a direct time-domain approach, the impedance can be modelled by a specific number of RC elements. Its analytical overpotential results in specific time constants as shown by Goldammer et al.[9] Segmented Fast Fourier Transformation (FFT) or Morlet Wavelet Transformation (MWT) are useful approaches for frequency-based impedance calculation. A problem is the non-flexibility regarding non-ideality of the test signal in real-world applications. Challenges regarding low-frequency time constants, measurement noise, inconsistency in the sampling frequency, non-linearity as well as self-discharging have to be considered. In the context of this work, realistic automotive measurement conditions refer to constraints typically encountered during cell-level or module-level testing of automotive lithium-ion cells, such as limited stabilization times, low sampling frequencies, non-ideal pulse shapes, measurement noise, and SOC-dependent OCV variations. These conditions differ from ideal laboratory pulse experiments, but they still represent controlled test scenarios rather than arbitrary in-vehicle load profiles. Highly dynamic current profiles during actual vehicle operation, including inverter-induced ripple and other drivetrain-related disturbances, are therefore beyond the scope of this study. However, the optimizations introduced here are a necessary step toward handling such non-ideal excitation signals. Provided that the current profile is measured with sufficient accuracy and sampling rate.

This work focuses on the pulse-fitting methodology developed by Schmidt et al.[10] (which for sake of completeness and reference has been summarised in the supplementary material) and its optimization as an alternative approach to deal with the described challenges. The method is based on fitting a physically motivated RC network to the measured voltage response of current pulses. In this work, the original algorithm is systematically enhanced by using systematic test pulse signals to address key challenges, including non-ideality of the measurement pulse, non-linearity due to SOC variations during the pulse, measurement noise, and limited stabilization times. Furthermore, the impact of sampling frequency and solver formulation is explicitly considered by adapting the underlying optimization approach.

The proposed improvements are evaluated using both synthetic and experimentally obtained pulse signals, demonstrating that reliable **ultra-low frequency** impedance information can be extracted without the need for additional, dedicated impedance measurements. The resulting methodology enables a robust determination of cell-specific diffusion characteristics and time constants correlating with the electrode specific phase change characteristic. As such the methodology represents a valuable extension to EIS measurements, which are typically performed at higher frequencies then applied here. This provides a valuable basis for advanced state estimation and model development in e.g. automotive battery applications.

Pulse-Fitting

Battery cells are capacitive systems that can be described in the time domain employing a high number of RC elements, even without extensive prior system knowledge. Utilising a current pulse, Schmidt et al.[10] developed an effective time-discrete algorithm for short pulse signals calculating the impedance as described in detail in the supplementary material.

The detectable system specific time constants (resolvable frequency range) is being limited by the steepness of the pulse edges, the sampling frequency and the measurement time during signal stabilization.[8]

Based on the Nyquist-Shannon sampling theorem, the minimum detectable time constant is defined by Shannon,[11]

$$\tau_{\min} \sim \frac{1}{\pi f_s} \qquad [1]$$

where f_s represents the sampling or measurement frequency. In practical applications, greater robustness is achieved by applying a safety factor. Schmidt et al.[10] utilize a value of $\tau_{\min,\,\text{safety}} = \frac{SF}{\pi f_s} = \frac{100}{\pi f_s}$.

The influence of the safety factor is exemplarily shown on a measurement pulse for a plug-in hybrid automotive cell in Fig. 2, the cell characteristics are published by Yin et al.[12] This measurement was performed at 25 °C, a discharging pulse with 1 C is used for 180 s with a starting SOC of 30% (ending SOC of 25%). Figure 2 illustrates the influence of the safety factor on the high-frequency impedance characteristic. To facilitate a clearer illustration and comparability, the focus is on the calculation and comparison of the Distribution of Relaxation Times (DRT). This visualisation proves more effective for identifying system dynamics compared to a direct comparison of impedance spectra in Nyquist or Bode plot. The peak with the highest frequency results mainly from ohmic effects,

[a]A list with the abbreviations and symbols used throughout this paper is given at the end of the paper

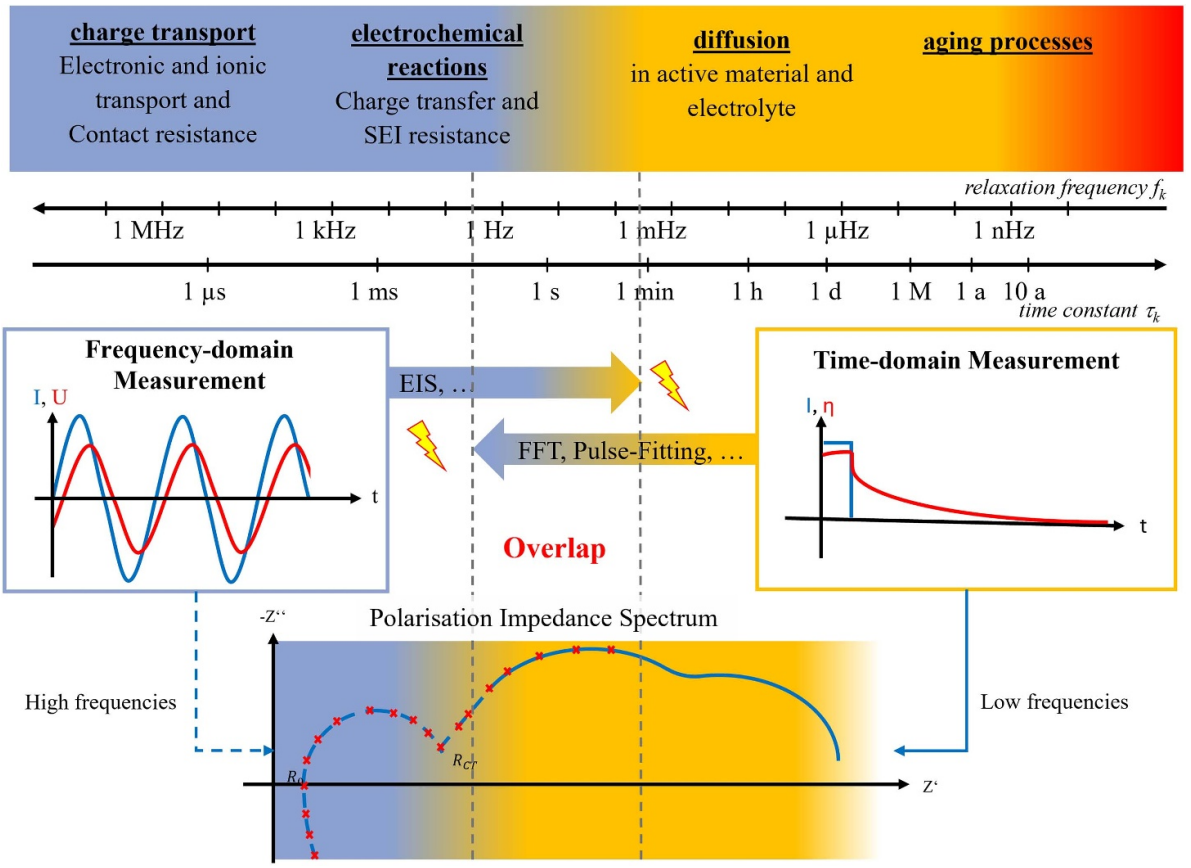

Figure 1. Overview over the system specific time constants of a battery cell. The typical measurement principles are separated into frequency-domain measurements (e.g. EIS) and time-domain measurements (e.g. FFT, MWT and Pulse-Fitting).

electrolyte conductivity as well as charge transfer effects. In the calculation algorithm, this is represented by the fitted RC element with the lowest time constant.

As can be seen, the two peaks at the lowest frequency (10^{-5}–10^{-4} Hz) neither changes location nor signal, whereas the double peak at 10^{-3}–10^{-2} Hz becomes far more resolved at a τ of 100 and the peak at 0.1 Hz present for $\tau = 1$ is not seen for $\tau = 100$. In this case, the peak at the highest frequency is significantly shifted to lower frequency. The influence on the calculated impedance increases by choosing higher safety values, however, calculation robustness results also increase. As will be shown in Section 4, in addition the sampling frequency has also to be considered.

Employing an iterative process regarding robustness and minimal influence on the processes, a safety factor of 4 has been found to be the optimum (Eq. 2). Here, the influence of $\tau_{\min}$ on the time constants with the highest values is negligible as shown in Fig. 2,

$$\tau_{\min} \sim \frac{4}{\pi f_s}. \qquad [2]$$

Additionally, the $\tau_{\max}$ values should be chosen larger than the largest time constant. It is noted, that process time-constants exceeding the maximum measurement time constant are the result of extrapolation. For short stabilization periods or poor measurement conditions, these extrapolated values are merely estimates and are subject to significant calculation errors (see Section 4).

For the considered time range from $\tau_{\min}$ to $\tau_{\max}$, this interval is discretised into 70 logarithmically spaced time constants.

The original application of this algorithm was not intended for automotive-specific challenges, such as long pulse periods, insufficient edge steepness, signal noise, low sampling rates typical for Cell Management Controller (CMC) recording, or short stabilization times. Furthermore, the procedure is highly sensitive to non-ideal pulse conditions. While an adaptation regarding signal noise was

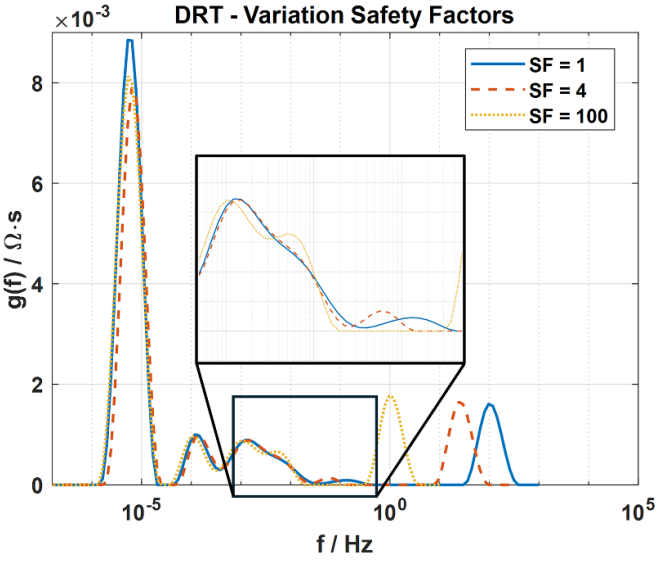

Figure 2. Influence of a $\tau_{\min}$ safety factor of 1, 4 and 100 on the impedance based DRT charactersitic. Pulse measurement at 25 °C, 30% starting SOC, 1 C discharging for a pulse duration of 180 s.

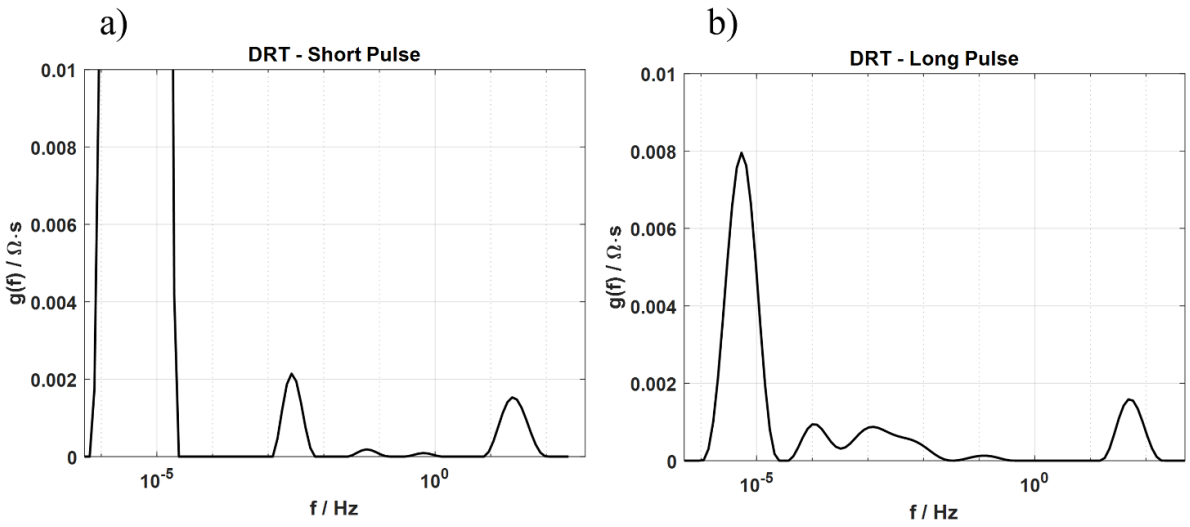

Figure 3. Comparison of the impedance-based DRT characteristic of two different pulse measurements at 25 °C, 1 C discharging and SOC level during stabilization of 25%. In a pulse duration of 1 s, in b 180 s.

previously implemented by Schmidt et al.[10] additional modifications to enhance flexibility and robustness are introduced in Section 4.

Simulation and Test Pulse Signals

All the presented computations are performed using MATLAB Version 2024b, employing self-developed algorithms on a HP laptop. The slight computational complexity enables a real-time calculation on e.g. BMS systems.

As described in Section 2, the application of the pulse-fitting method requires short current pulses followed by sufficiently long stabilization periods, high and constant sampling frequencies and the fulfilment of linearity criteria. These requirements significantly constrain the method´s utility, both in the development process and in-vehicle applications. Furthermore, when coupled with frequently insufficient polarization (too small for an excitation peak), the diagnostic value of such pulses remains limited.

As an example, Fig. 3 shows the influence of a discharge pulse length (1 s vs. 180 s at 1 C, yielding in a state of charge difference of 0.03%–5% respectively) and the amount of charge quantity on the triggered time constants in the impedance characteristic of the mentioned automotive cell from Yin et al.[12] It should be noted that 1 C is exceeding typical stimulation amplitudes in conventional EIS and will most probably trigger nonlinear contributions in the response.

In a, the short excitation current causes problems in the boundary value calculation at low frequencies as well as the absence of a trigger for the relevant long term electrochemical processes. In comparison, the subfigure b shows the impact of higher discharging quantity in triggering different processes.

This demonstrates that there is no one-size-fits-all pulse signal applicable for any type of cell. Instead, the pulse design must be adapted to the cell chemistry, operating point, measurement constraints, and the electrochemical processes of interest. Therefore, robust pulse-fitting methods must be able to handle non-ideal and application-specific pulse signals rather than relying on a predefined ideal excitation. In practice, the appropriate pulse signal depends not only on the cell itself, but rather on the specifications and selected settings of the cell test system used.

For the short pulse, the calculated impedance mainly represents the SOC inhomogeneity within the electrode between current collector and separator. For the long pulse, the main impedance impact is caused by solid state diffusion. The resolution and accuracy have to be considered in the same way as the importance of a sufficient excitation for a robust and reproducible impedance calculation.

To enhance the methodology to conditions not meeting ideal laboratory requirements (as e.g. is typical in a vehicle environment), specific adaptations of the pulse-fitting algorithm (as described in Section 2) were derived. Tests of the improved description were performed employing pulse signals derived from Open Circuit Voltage (OCV) measurement which by their nature inherently do not meet ideal measurement requirements (e.g. due to noise). Yet they do represent the real world and are as such the ultimate test for the proposed method.

As a way of illustration, Fig. 4 shows the OCV measurement for the afore-described automotive cell at 1 C and a SOC step size of 2.5% also used for the analyses in Section 5. These measurements were performed employing a MACCOR Cell Test System Series 4000-TXE000A with a voltage accuracy of 1.2 mV, a current accuracy of 0.06 A, a sampling frequency of 1 Hz and an adjustment of the current to the setpoint within 20 ms. The cells under measurement were placed in a CTS C-40/350 climate chamber, stabilized at 25 °C. All measurements were performed employing a standard in house profile consisting of:

- 3 consecutive capacity measurements (I) at 1 C
- A stepwise discharging (II), which is terminated on the basis of the coulombic charge being discharged in steps of 2.5% SOC. The discharge rate being 1 C until the CV limit was reached. At that moment, the current was dynamically changed to maintain the CV-limit.
- Charging sequence (III). Charging was performed employing the same protocol as for the discharging (II).

The next SOC step is initiated when the voltage stabilization rate falls below a predefined threshold of 0.2 mV h^{-1} (not shown in Fig. 4).

Each of these SOC steps constitutes a pulse measurement suitable for the pulse-fitting analysis. Three generic and representative single pulse signals (Signal A, B and C) are also shown in Fig. 4 (for the sake of clarity, it is noted that the pulses do not reach equilibrium in this inset). This methodology facilitates the identification of small time constants and internal balancing processes within the cell.[13]

The generic signals illustrated in Fig. 4 are simulated employing an equivalent circuit consisting of 3 RC elements with different time constants and thus representing idealised conditions specified in Table I (Pulse Signal A). For the simulations, a charging and discharging specific OCV characteristic is described by a linearised

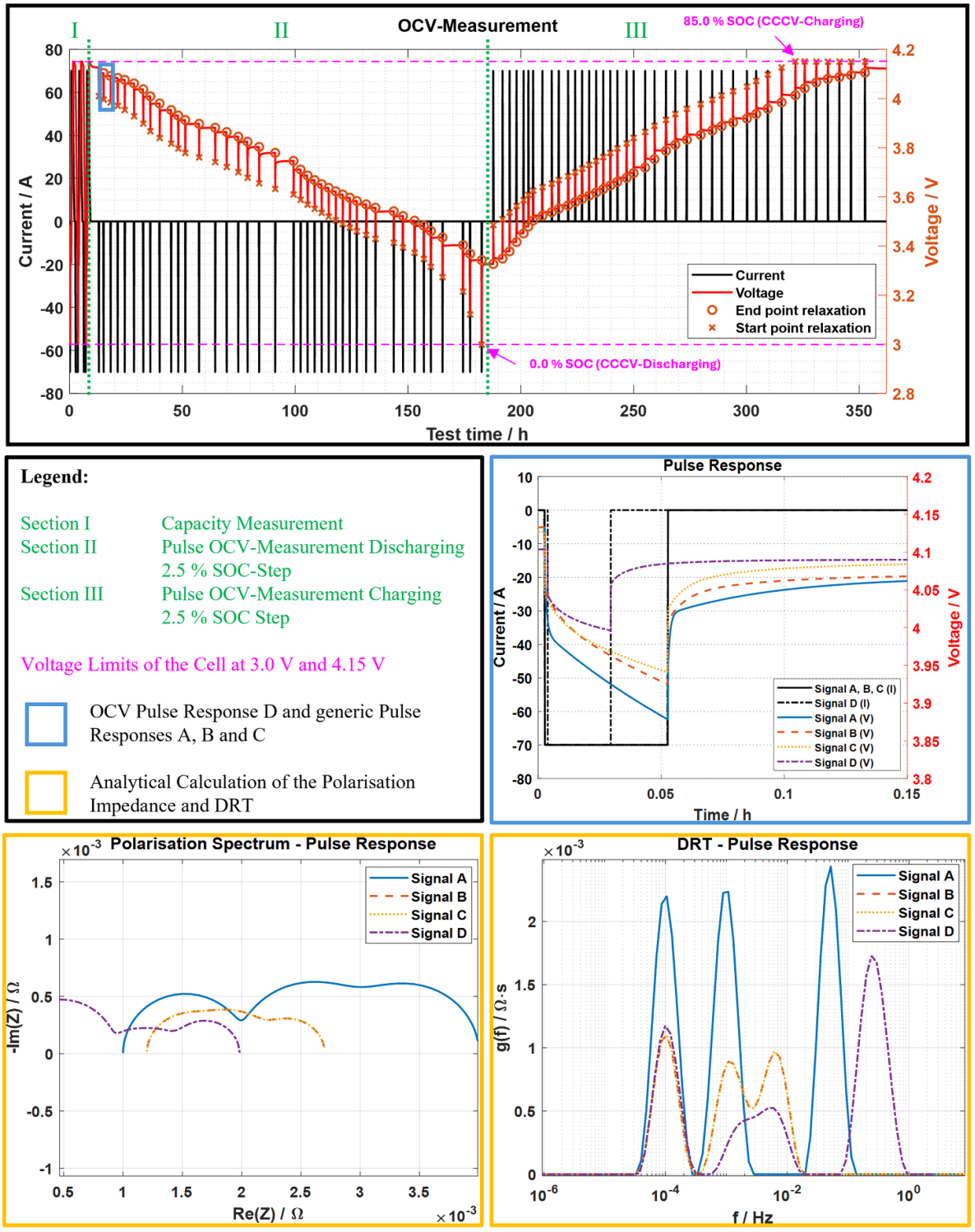

Figure 4. OCV measurement principle. Capacity measurement (I) followed by pulsation testing (II + III). Stepwise discharging followed by stepwise charging. The switch to CV charging and discharging is highlighted. Initial part of the used generic pulse signals, refering to a discharge pulse measurement at 95% SOC, are shown in the blue framed boxes with analytical impedance calculation and subsequent DRT computation highlighted in the orange framed boxes.

Table I. Generic test pulse Signal A and adaptation in Signal B and C for a realistic test case. Signal D describes a pulse-measurement on a full cell. Deviations between the different signals, compared to Signal A are highlighted in bold.

Pulse Response Signal	A	B	C	D
Number of RC elements	3	3	3	
Frequencies RC elements	$5 \cdot 10^{-2}$Hz	$6.5 \cdot 10^{-3}Hz$	$6.5 \cdot 10^{-3}Hz$	
	$1 \cdot 10^{-3}$Hz	$1.15 \cdot 15^{-3}Hz$	$1.15 \cdot 15^{-3}Hz$	
	$1 \cdot 10^{-4}$Hz		$1 \cdot 10^{-4}$Hz	
Resistances RC elements	1 mΩ	0.5 $m\Omega$	0.5 $m\Omega$	
Ohmic-resistance	1 mΩ	1.2 $m\Omega$	1.2 $m\Omega$	
Cell capacity	70 Ah	70 Ah	70 Ah	Pulse measurements on a full cell. (mainly used 97.5% to 95.0%)
Pulsation current	−70 A	−70 A		
Pulsation duration		180 s	180 s	
Pre-pulsation time	10 s	10 s	10 s	
stabilization time	40000 s	7600 s	7600 s	
Sampling rate	10 Hz	1 Hz	1 Hz	
OCV characteristic	Generic, linear (Eq. 3)	Generic, linear (Eq. 3)	Realistic, extracted from measurement	

approach according to Eq. 3,

$$U_{\text{OCV\_generic\_test}} = 4.133V + 1.2 \cdot (\text{SOC} - 1) \quad [3]$$

Subsequently, to create a more realistic test case, the pulse signal is adapted by using more realistic time constants based on the cell measurements. These adaptations are detailed in Table I (Signals B and C).

In Signal B, the RC frequencies, resistances and stabilization times are adjusted to represent a more authentic, yet more challenging, test scenario. Furthermore, the sampling frequency is reduced, resulting in time constants that are no longer distinctly separated. Signal C incorporates an OCV characteristic extracted directly from cell measurements. Both signal adaptations increase the risk of ambiguity within the solver's solution. Finally, physical measurements (Signal D) are utilized as fourth test signals. Here, an additional peak in the DRT-plot at high frequencies is caused by the sampling frequency and the applied pulse-fitting calculation, explained in Section 2.

Optimization of the Pulse-Fitting Algorithm

As previously explained, the classical pulse-fitting method as described in Section 2 is unable to reliably extract the impedance and diffusion characteristics when applied to more complex, real-world, test signals such as described in Section 3. To adapt the pulse-fit methodology to such more complex and real-world signals, the method was further developed by employing the following optimizations:

- Numerical calculation of the current matrix A instead of using the analytical solution of a square wave signal.
- Extension of the kernel matrix to account for non-linearities caused by changes in the SOC state during the pulse phase.
- Tikhonov regularisation to reduce the influence of amplified noise components on the measurement.
- The application of diagonal weights in the context of matrix scaling for robustness against varying measurement frequencies and error contributions for the least-squares fit problem.
- The introduction quadratic programming as an alternative solver, to increase the stability of the solution set compared to the classical least-squares fit problem.
- Extrapolation of individual relaxation processes in the case of excessively short stabilization times.

For the sake of traceability, all adaptations are evaluated against the reference test signals from Section 3 Table I. In all following subsections, the calculation results of the origin methodology are directly compared with the calculation by using the optimized strategies.

Numerical convolution.—The use of the analytical solution for the voltage characteristic described in Section 2 requires the application of an ideal rectangular pulse. If this condition is not met, the solution set will be erroneous. In real-world applications, the rectangular pulse cannot always be guaranteed. Boundary conditions regarding maximum permissible current as well as adherence to cell voltage limits necessitate current reduction in the edge regions of the SOC window in discharging as well as in charging direction. Non-constant current profiles, classified by the transition from CC to CV phases, are the result.

To nonetheless compute reliable impedance results under real conditions, a numerical convolution of the RC elements is employed. The recursive time-discrete numerical solution of the entries of matrix **A** corresponds to Eq. 4 replacing Eq. S.8 (supplementary material). Subsequent calculation steps remain unchanged,

$$a_j(i) = a_j(i-1) \cdot e^{-\frac{\Delta t}{\tau_j}} + i_P(i-1) \cdot \left(1 - e^{-\frac{\Delta t}{\tau_j}}\right). \quad [4]$$

The influence of the current signal shape as it occurs in the CV charging phase (87.5%–90.0% compared with the last CC Phase Peak at 85% SOC) for both the analytical and numerical solution methods is illustrated in Fig. 5. As shown in Fig. 5.c, the charging voltage reaches its upper voltage limit of 4.15 V. As a consequence, the OCV measurement proceeds with a CV step until the entire charging amount is reached. Compromising the shape from a rectangular to at least a partly exponential shape. Using the numerical solution in Subfigure b, the impedance solution and resulting DRT calculation becomes more stable than using the analytical solution in Subfigure a. As shown by Levi et al.[14] the slow processes, mainly the diffusion processes, change in the time-constant dependent on the intercalation level. Within a SOC change of 5%, only slight changes in the characteristic are expected and also revealed in Subfigure b. A change of the fast process time constant, mainly caused by variations in the charge transfer are negligible here. The usage of a numerical approach results in a traceable impedance calculation.

The numerical convolution is not restricted to ideal rectangular pulses but can by principle be applied to any measured current profile, as long as the current and voltage signals are

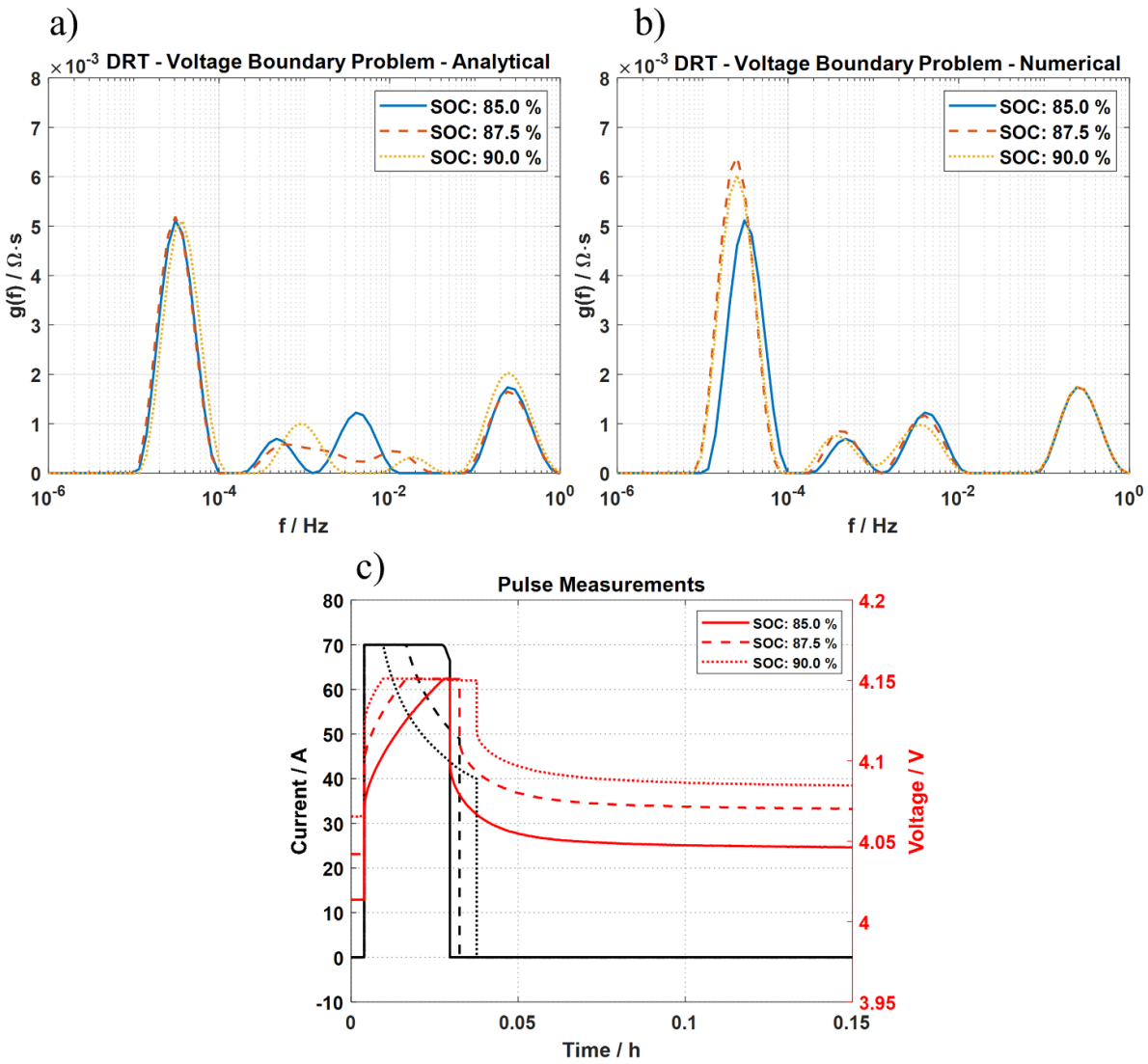

Figure 5. Comparison between the analytical and numerical solutions for non-ideal pulse conditions (CCCV charging) at 87.5% and 90.0% SOC as well as nearly ideal pulse conditions (CC charging) at 85.0% SOC.

recorded with sufficient sampling rate, accuracy and synchronisation. This is an important prerequisite for future applications involving more complex excitation patterns, such as dynamically varying load profiles. However, the present study validates the approach using controlled (automotive) cell test signals and CCCV-related non-ideal pulse shapes. Additional work is required to assess the robustness of the method under actual in-vehicle current profiles, including disturbances such as high-frequency ripple components or drivetrain-induced disturbances.

Augmentation of the Kernel matrix.—To mitigate the problem of non-linearity, one way would be to construct each SOC-specific pulse to (infinite) small rectangular pulses. However, simplifying the analysis to a linear system by using short pulses, thereby only marginally altering the system characteristic, is limiting and fails to stimulate slow electrochemical processes. In addition, the use of a fixed OCV characteristic for pulse-fitting, as described by Eqs. S.9 and S.10 (supplementary material), is only suitable for short pulse durations or low currents with neglectable SOC changes. Applying this simplification to high pulse currents or extended durations result in a boundary value problem for small time constants.

As the OCV varies depending on the SOC, Eq. S.9 (supplementary material) has to be adapted to the form given in Eq. 5. Incorporating the dependencies of the time-discrete open-circuit voltage on SOC, temperature and charging direction (hysteresis) resolves the described problem. The dynamic OCV characteristic during SOC variation (OCV_{before} and should be utilized as $V_{\text{OCV, dyn}}(t)$ for an adapted time-discrete calculation in accordance with Eq. 5,

$$\left[\; A \; \boldsymbol{U}_{\text{OCV}_{\text{dyn}}} \;\right] \cdot \begin{bmatrix} R \\ 1 \end{bmatrix} = \boldsymbol{u}. \qquad [5]$$

Notwithstanding the above, determining the state-specific start and end voltages of a cell system remains difficult due to non-idealistic steady-state conditions. Additionally, hysteresis characteristics of the electrode systems have to be considered. As reported by Heß et al.[15] different staging sequences during charge and discharge of graphite will be passed through, and not every phase is suggested to occur in both directions. Didier et al.[16] explain this by different kinetic barriers between the stages of graphite. Complete equilibration is practically impossible due to minimal entropy differences combined with existing kinetic barriers.[15,16] Deviations from the correct OCV

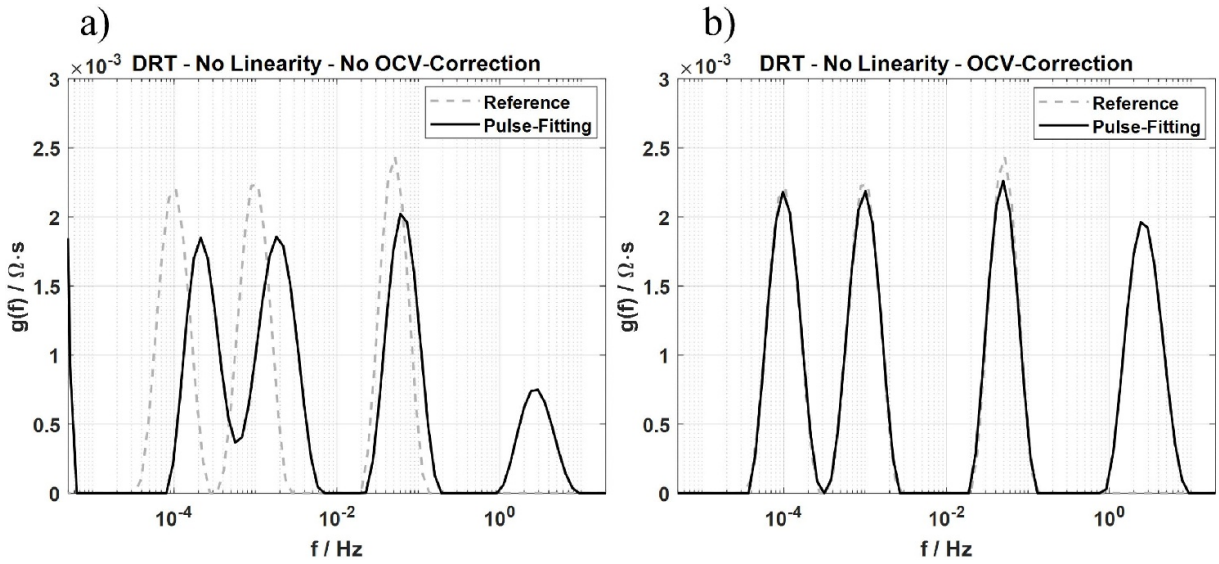

Figure 6. DRT of a pulse-fitting impedance calculation. In a without dynamic OCV correction and in b with dynamic OCV correction.

characteristic lead to erroneous calculations. To address this, two distinct approaches are possible:

1. Using the OCV values before the pulse and after voltage stabilization directly. This requires steady state conditions before and after the pulsation test. Alternatively, an extrapolation approach can be used.
2. By knowing the correct SOC level from accurate ampere-hour counting and capacity calculations in combination with historic memory data:

Under usage of either approach, and based on Eq. 5, Eq. S.10 (Supplementary Material) can be transformed to:

$$\begin{bmatrix} a_{1,1} & \cdots & a_{1,N} & U_{\mathrm{OCV_{dyn}}} \\ \vdots & \ddots & \vdots & \vdots \\ a_{M-1,1} & \cdots & a_{M-1,N} & U_{\mathrm{OCV_{dyn}}\,M-1} \\ a_{M,1} & \cdots & a_{M,N} & U_{\mathrm{OCV_{dyn}}\,M} \end{bmatrix} \cdot \begin{bmatrix} R_1 \\ \vdots \\ R_N \\ 1 \end{bmatrix} = \begin{bmatrix} u_1 \\ \vdots \\ u_{M-1} \\ U_M \end{bmatrix}. \quad [6]$$

The summation of matrix **A** and vector $U_{\mathrm{OCV_{dyn}}}$ leads to a new matrix **B**. Applying the least-squares fit algorithm yields the minimal solution, as expressed in Eq. S.11 (supplementary material). The interpretation of the last entry of vector **x** depends on the specified calculation matrix employed.

When utilising Eq. S.10 (supplementary material), this entry describes a fixed calculated OCV voltage point of the system. Alternatively, employing Eq. 6, the last entry of vector **x** can be seen as a control parameter. If an optimal OCV curve is used, this last entry results in a coefficient of 1.

The effect of omitting the OCV value correction during time-discrete calculation is illustrated in Fig. 6. The plots reveal a boundary value problem at the lowest calculated frequencies when using the generic Signal A from Table I. For this study, the signal itself has no impact on the functionality of the compensation methodology, and the simplest test signal has been used. Consequently, calculating the impedance in real-world applications without the requirement of an ideal short pulse signal, necessitates a dynamic OCV correction.

Tikhonov regularisation.—The robustness against noisy measurement signals and calculation errors can be increased by using the second derivative of the resistance values and multiplying it with the solving matrix.[17] The time-discrete second derivate can be calculated using Tikhonov regularisation, which is a widespread tool for discrete deviation calculation and the improvement of calculation robustness, as shown exemplarily by Weese[18] and Gavrilyuk et al.[19] A weighted form of this approach is presented in Eq. 7.

$$\frac{d^2R_n}{dn^2} \approx -0.5R_{n-1} + 1R_n - 0.5R_{n+1}. \quad [7]$$

The multiplication matrix using the methodology of Eq. 7 results from the form $[N+1\ x\ N]$ to Eq. 8.

$$I_{\mathrm{reg}} = \begin{bmatrix} 1 & -0.5 & 0 & \cdots & 0 & 0 \\ -0.5 & 1 & -0.5 & \ddots & \vdots & \vdots \\ 0 & -0.5 & 1 & \ddots & 0 & \vdots \\ \vdots & \ddots & \ddots & \ddots & -0.5 & \vdots \\ 0 & \cdots & 0 & -0.5 & 1 & 0 \end{bmatrix}. \quad [8]$$

Adapting Eq. S.11 (supplementary material) and employing a weighted form of Eq. 8 yields in Eq. 9. Schmidt et al.[10] are using the weighting factor $\lambda\frac{M}{N}$ for sampling rate and data point compensation

$$\min_x \left\| \begin{pmatrix} \mathbf{B} \\ \lambda\frac{M}{N}\mathbf{I_{reg}} \end{pmatrix} x - \begin{pmatrix} \mathbf{u} \\ 0_{N+1} \end{pmatrix} \right\|_2^2 \text{s.t.} R_n \geqslant 0. \quad [9]$$

The robustness against poor signal quality is tested by the artificial summation of the pulse signal B, as this consists of realistically spaced time constants with random noise employing perturbations of: 0 mV, 0.1 mV, 0.2 mV, 0.5 mV, 2.0 mV and 5.0 mV. Here, the influence of a realistic OCV-characteristic of Signal C in comparison to the generic OCV of Signal B is neglectable by using a random noise perturbation. For reasons of simplification, Signal B is used.

The impedance calculations performed without the regularisation adaption are shown in Fig. 7a. For high perturbations, the solutions become unstable as indicated by the shift of peak frequency for the peaks with 2 and 5 mV. Additional boundary value problems are a consequence. The results obtained using Tikhonov regularisation are shown in Fig. 7b. The time constants of the generic signal are clearly evident in the corresponding DRT peaks. While the influence of the

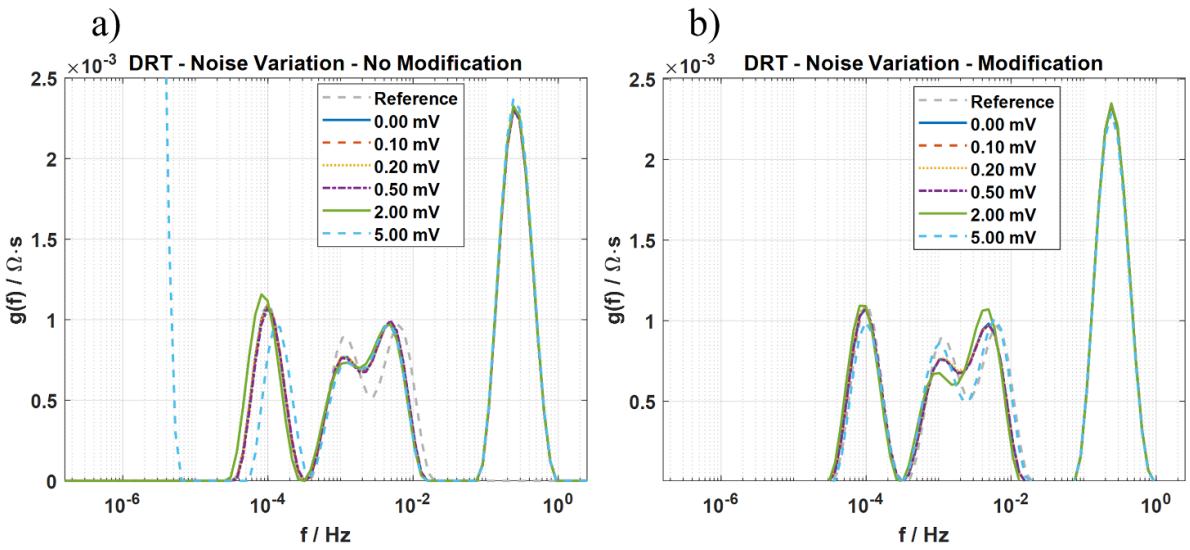

Figure 7. DRT calculation of the generic Signal B. Different noise levels are used to evaluate the influence on the impedance. In a: DRT without Tikhonov regularisation. In b: DRT employing Tikhonov regularisation.

noise level is visible across all processes, especially the higher time constants are influenced by high noise perturbations. Nevertheless, the time constants of all RC elements remain stable and reproducible.

In summary, Tikhonov regularisation stabilizes the deconvolution within the measured frequency band as determined by the relaxation times.

Diagonal weighting and column scaling.—While in a laboratory environment sampling rates are basically only limited by the used measurement equipment and can be up to the kHz range in an automotive environment, not only are far more cells to be measured at the same time (easily of the order of several hundreds), due to cost constrains a typical sampling rate of low Hz down to sub-Hz level are typical. To study the influence of the measurement frequency, Signal A is utilized, while mathematically reducing the frequency down to 2, 1 and 0.2 Hz compared to a base frequency of 10 Hz.

Robustness requires that the DRT solution is independent of the measurement frequency. However, for a given time domain the first term of Eq. 9, specifically the term $\|\boldsymbol{Bx}-\boldsymbol{u}\|^2$, increases proportionally with the number of data points M. By adapting a weighting factor, it can be prevented that segments are being over-weighted due to the squaring of the least-squares fit problem by using different sampling frequencies for the same signal characteristic. In other words: Every part of a test signal, regardless of varying sampling frequencies during measurement, maintains the same relative weight in the fitting algorithm. Consequently, with regard to Eq. 9, the mathematical problem remains invariant to changes in the sampling frequency.

The individual elements, $\boldsymbol{B}$ and $\boldsymbol{u}$, have to be weighted by $W = \mathrm{diag}\left(\sqrt{\Delta t_1}, \sqrt{\Delta t_2}, \ldots, \sqrt{\Delta t_M}\right) \in \mathbb{R}^{M\times M}$, which results in Eq. 10:

$$\boldsymbol{B_w} := \boldsymbol{W}\cdot\boldsymbol{B} \text{ and } \boldsymbol{u_w} := \boldsymbol{W}\cdot\boldsymbol{u}. \qquad [10]$$

With this adaption, the least-squares fit calculation corresponds to the mathematical useful approximation in Eq. 11.

$$\sum_{i=1}^{M}\Delta t_i\left(\left(B_w x\right)_i - u_i\right)^2 \approx \int\left(u_{\mathrm{model}}\left(t\right) - u_{\mathrm{mess}}\left(t\right)\right)^2 \mathrm{d}t. \qquad [11]$$

And the second part of Eq. 9 can be adapted to:

$$\frac{\lambda M}{N}\|\boldsymbol{I}_{\mathrm{reg}}x\|_2^2 \rightarrow \lambda_{\mathrm{fix}}\|\boldsymbol{I}_{\mathrm{reg}}x\|_2^2 \qquad [12]$$

A fixed weighting factor of $\lambda_{\mathrm{fix}} = 0.2$ is employed for described test cases by using the L-curve-method.

In matrix notation, the least-squares fit problem can be described as:

$$\min_x\left\|\begin{pmatrix}\boldsymbol{B_w}\\ \lambda_{\mathrm{fix}}\boldsymbol{I_{reg}}\end{pmatrix}x - \begin{pmatrix}\boldsymbol{u_w}\\ 0_{N+1}\end{pmatrix}\right\|_2^2 \quad \text{s.t. } R_n \geqslant 0. \qquad [13]$$

An additional optimization can be achieved through column scaling. By scaling the columns of matrix $\boldsymbol{B_W}$, all column vectors are normalised to a unique size 1 using a scaling factor, S. This improves the robustness and prevents a wide spread of eigenvalues within the matrix $\boldsymbol{B_W^T B_W}$. Consequently, the condition number of the normal equation matrix is significantly reduced. This approach effectively mitigates issues related to poor convergence and rounding errors within the least-squares fit problem. Furthermore, the required computing time is significantly reduced. For all columns, the Euclidean norm is calculated according to Eq. 14,

$$v_j = \|\left(B_w\right)_{:,j}\|_2 = \sqrt{\sum_{i=1}^{M}\left(B_w\right)_{ij}^2}, j = 1,\ldots,N+1. \qquad [14]$$

The dialog scaling matrix can be rewritten to Eq. 15, where ε avoids a division by 0.

$$\boldsymbol{S} = \mathrm{diag}\left(\frac{1}{\max\left(\nu_1,\varepsilon\right)},\ldots,\frac{1}{\max\left(\nu_{N+1},\varepsilon\right)}\right) \in \mathbb{R}^{(N+1)\times(N+1)}. \qquad [15]$$

The least-squares fit calculation of the adapted matrix system, now being given by Eq. 16,

$$\min_y\left\|\begin{pmatrix}\mathbf{B_w S}\\ \lambda_{\mathrm{fix}}\mathbf{I_{reg}S}\end{pmatrix}y - \begin{pmatrix}\mathbf{u_w}\\ 0_{N+1}\end{pmatrix}\right\|_2^2 \text{s.t.} y \geqslant 0, \qquad [16]$$

and final back scaling step by:

$$\mathbf{x}^* = \mathbf{S}\cdot\mathbf{y}^*. \qquad [17]$$

The results in Fig. 8 demonstrate that the DRT calculation is improved by incorporating diagonal weighting and column scaling,

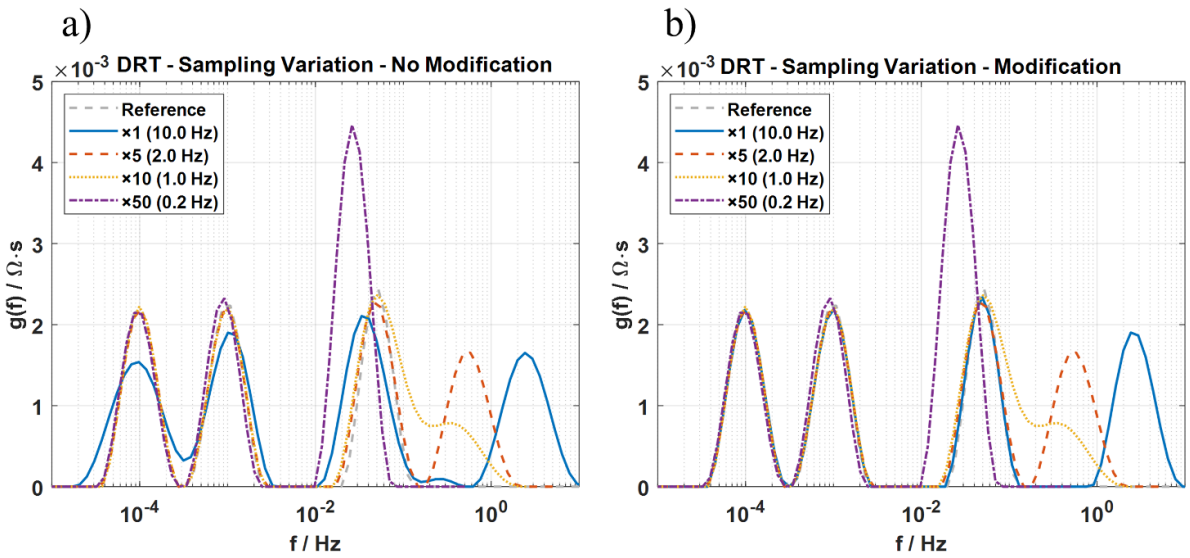

Figure 8. DRT calculation of the Signal A with variation of the sampling frequency. In a without and in b with diagnoal weighting and column scaling.

even when utilising a nearly ideal test signal (Signal A). An influence of the sampling frequency on the polarization impedances and their relative weighting is discernible, whereas the effect on the time constant itself is negligible. The differences between the various sampling frequencies are negligible. Only, for small time constants and low sampling rates, the results are not quite optimal, which is caused by the violation of the sampling theorem.

Quadratic programming.—Various methods can be employed to optimize the least-squares fit problem discussed in the previous subsections. These include numerical convolution, augmentation of the kernel matrix, Tikhonov regularisation, and the application of the aforementioned weighting and scaling factors, without optimizing the solver itself.

Garda et al.[20] utilized quadratic programming (QP) to achieve superior solution quality for their magnetic coil design problem. Similarly, the solving strategy for the current problem can be optimized by adopting a quadratic programming approach. For a better visualisation, $\boldsymbol{B}_{\mathrm{w}}$ instead of $\boldsymbol{B}_{\mathrm{w}}S$ is used for the following elucidations.

The general Eq. 18 describes the least-squares fit problem and can be substituted into the form of the QP problem in Eq. 19. The transformation steps of the Eqs. 20–22 are described afterwards.

In this context, both $\boldsymbol{B}_{\mathrm{w}}^{\top}\boldsymbol{B}_{\mathrm{w}}$ and $\boldsymbol{I}_{\mathrm{reg}}^{\top}\boldsymbol{I}_{\mathrm{reg}}$ are symmetric positive semi-definite. It should be noted, that this simplification to a positive definite matrix limits the matrix size $\boldsymbol{B}_{\mathrm{w}}$ to $M \geqslant N+1$. The matrix $\boldsymbol{I}_{\mathrm{reg}}$ (from Eqs. 7 and 8) could causes a null space. In this case, the rank of the matrix is not full. Therefore, the simplification to positive definite is not applicable in this case.[21]

$$\min_{y} \mathcal{J}\left(x\right) = \|\mathbf{B}_{\mathrm{w}}\mathbf{x} - \mathbf{u}_{\mathrm{w}}\|_2^2 + \lambda_{\mathrm{norm}}^2 \mathbf{I}_{\mathrm{reg}}\mathbf{x}_2^2 \qquad [18]$$

$$\min_{x} \frac{1}{2}\mathbf{x}^{\mathrm{T}}\mathbf{H}\mathbf{x} + \mathbf{f}^{\mathrm{T}}\mathbf{x}. \qquad [19]$$

With the sub-equations of 18 rewritten into:

$$\begin{aligned} \|\boldsymbol{B}_{\mathrm{w}}\boldsymbol{x} - \boldsymbol{u}_{\mathrm{w}}\|_2^2 &= \left(\boldsymbol{B}_{\mathrm{w}}\boldsymbol{x} - \boldsymbol{u}_{\mathrm{w}}\right)^{\top}\left(\boldsymbol{B}_{\mathrm{w}}\boldsymbol{x} - \boldsymbol{u}_{\mathrm{w}}\right) \\ &= \boldsymbol{x}^{\top}\boldsymbol{B}_{\mathrm{w}}^{\top}\boldsymbol{B}_{\mathrm{w}}\boldsymbol{x} - 2\boldsymbol{u}_{\mathrm{w}}^{\top}\boldsymbol{B}_{\mathrm{w}}\boldsymbol{x} + \|\boldsymbol{u}_{\mathrm{w}}\|_2^2 \\ \|\boldsymbol{I}_{\mathrm{reg}}\boldsymbol{x}\|_2^2 &= \boldsymbol{x}^{\top}\boldsymbol{I}_{\mathrm{reg}}^{\top}\boldsymbol{I}_{\mathrm{reg}}\boldsymbol{x}. \end{aligned} \qquad [20]$$

Inserting these into Eq. 18, yields:

$$\mathcal{J}\left(x\right) = \boldsymbol{x}^{\top}\left(\boldsymbol{B}_{\mathrm{w}}^{\top}\boldsymbol{B}_{\mathrm{w}} + \lambda_{\mathrm{norm}}^2\,\boldsymbol{I}_{\mathrm{reg}}^{\top}\,\boldsymbol{I}_{\mathrm{reg}}\right)\boldsymbol{x} - 2\boldsymbol{u}_{\mathrm{w}}^{\top}\boldsymbol{B}_{\mathrm{w}}\boldsymbol{x} + \|\boldsymbol{u}_{\mathrm{w}}\|_2^2. \qquad [21]$$

The part $u_{\mathrm{w}2}^2$ has no influence on the minimisation of the solution. So, it can be ignored. By comparing Eq. 21 with the target-shape of Eq. 19, it follows that:

$$\begin{aligned} \boldsymbol{H} &= \boldsymbol{B}_{\mathrm{w}}^{\top}\boldsymbol{B}_{\mathrm{w}} + \lambda_{\mathrm{norm}}^2\,\boldsymbol{I}_{\mathrm{reg}}^{\top}\boldsymbol{I}_{\mathrm{reg}} \\ \boldsymbol{f} &= -\boldsymbol{B}_{\mathrm{w}}^{\top}\boldsymbol{u}_{\mathrm{w}}. \end{aligned} \qquad [22]$$

With the physically implied constraint $R_n \geqslant 0$, an interior-point algorithm can be employed to solve this problem. characterized by quadratic convergence and robustness in the presence of ill-conditioned problems (such as the extrapolated frequency range of the impedance), quadratic programming improves the stability of the solution and helps to mitigate boundary value problems.[22,23]

For demonstration purposes, Signal A, which contains a stored generic OCV characteristic, is processed using the pulse-fitting method without OCV adaptation. This to deliberately induce a boundary value problem (as seen in Fig. 6a at low-frequency). Transitioning to the quadratic programming solver significantly reduces this boundary value problem and enhances the stability of the solution set, as illustrated in Figs. 9a and b. Nevertheless, a residual error remains.

DRT stabilization.—The fading slope of the voltage stabilization (overpotential) is caused by decaying polarization effects, such as solid-state diffusion, phase-change effects, mechanical anode overhang. Depending on the signal stabilization history and the potential level, different effects may dominate, their relative contribution even changing within the measurement time. In real-world applications, due to practical reasons, the stabilization time is often shortened in comparison to laboratory use-cases. A highly relevant aspect for automotive cell testing and as a prerequisite for future in-vehicle diagnostics. The resulting ill conditioned problem results in ambiguities regarding low-frequency time constants for impedance calculations. In this subsection, an extrapolation approach of the DRT using impedance changes as a consequence of repeatedly artificially shorted stabilization times of the test pulses is used to stabilize the DRT calculation.

To demonstrate the impact of varying voltage stabilization times on the impedance characteristic, the following slope gradients were

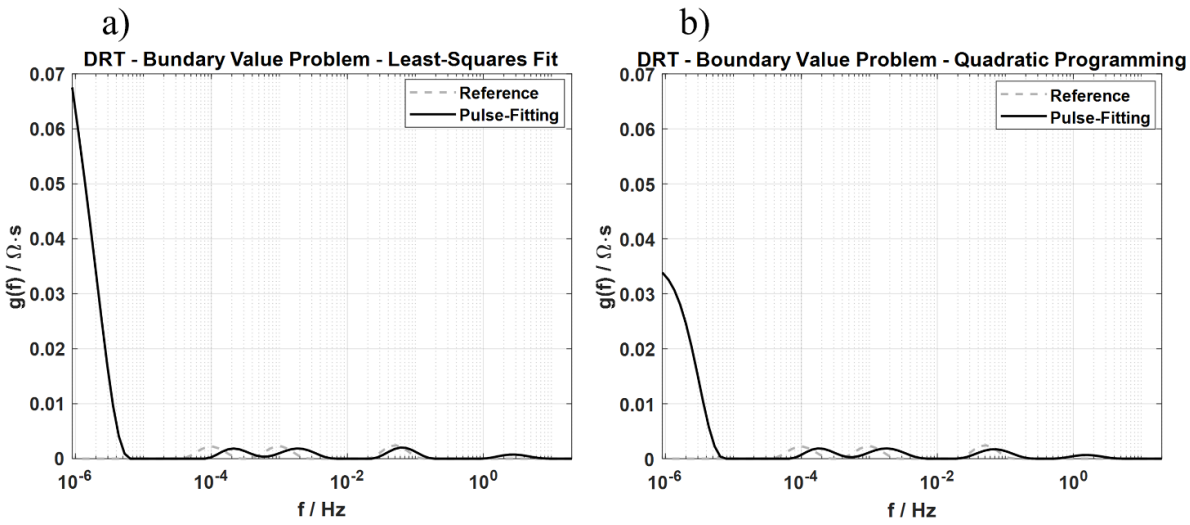

Figure 9. DRT calculation of Signal A with induced boundary value problem; employing a least-squares fit solver in a and a quadradratic prgramming solver in b.

used to truncate the test signals from Table I: 2.00 mV h^{-1}, 1.00 mV h^{-1}, 0.50 mV h^{-1} and 0.25 mV h^{-1}. The DRT subsequently being calculated for each of these constrains (durations).

For the ideal generic signal (Signal A), the time constants are sufficiently separated such that the algorithm fits them without difficulties (see Fig. 10a). Consequently, the slope gradient and stabilization duration have no significant influence on the calculation.

However, employing the generic signal with more realistic time constants (Signal B), it is evident from Fig. 10b that the low-frequency DRT amplitude changes. Both the time-constants and their spectral positions influence the calculation´s sensitivity to short stabilization times. Using the most realistic generic signal (Signal C), it is clear that the adaptation to a real OCV characteristic further impairs stability as the end of voltage stabilization time is chosen too early (and hence a too-short stabilization time). As demonstrated in the previous subsections, it is neither the influence of the signal noise nor the quantity of measurement points that primarily affects the calculated DRT, but rather a measurement duration, long enough to detect all the processes associated with long halftime constants. A similar effect is observed for the measurement signal (Signal D), showing that the considerations based on artificial signals can also be transformed to realistic measurements.

This brings about the question of how to deal with measurements that in retro-perspective were too short. Since this implies extending the frequency range under consideration into extrapolation, a correlation to corresponding measurements no longer exists, the pulse-fitting calculation becomes increasingly unstable and tends to boundary value problems. Nevertheless, Figs. 10a–d demonstrate a converging DRT in correlation to an increasing stabilization time.

By using the synthetic Signal C, the stabilization time was artificially extended by a factor of 10 in a first step. The resulting DRT is illustrated in Fig. 10e. As will be clear from this comparison, the influence of extending the stabilization times is negligible under this condition.

To mitigate the calculation problem associated with short stabilization times and varying impedance calculations, several extrapolation strategies were tested.

An extrapolation of the overpotential characteristic directly or an extrapolation of the impedance itself is not useful, since slow processes as such are not observed in this process, or at least underestimated. For a correct extrapolation, different time constants have to be assumed.

Considering the above-mentioned issues, an alternative route has been employed: utilising a linear regression shown in Eq. 23 an extrapolation to infinite stabilization times is possible.

$$y = b_0 + b_1 \cdot x$$
$$\text{with } x = \frac{1}{\text{stabilization\_time}}. \qquad [23]$$

To generate the pair of values (extrapolation base), the impedance and DRT at different slope gradients of the stabilization time is calculated, already shown in Figs. 10a–d. The intercept of the regression, calculated with the MATLAB-algorithm *robustfit,* describes the DRT-calculation point for an infinite stabilization time. The extrapolation of the extended Signal C (shown in Fig. 10e) while using varying stabilization times is shown in Fig. 10f. Here, the extrapolated impedance is much more stable than solely using the shortened signal with the specific slope gradients. By using the entire stabilization time, the extrapolated DRT converge to the direct calculated DRT in Fig. 10e. As shown, a deviation remains.

Impedance Calculation; Application to Automotive Cells

After the previous theoretical derivation and testing on rather synthetic signals, the applicability of the method to realistic large capacity batteries is studied in this Section. Employing the cells and measurement conditions described in Section 3 and a change in voltage < 0.2 mV h^{-1} as end criterium, both in discharge and charge direction. The presented results are a first scope. A more detailed analyses, including temperature-dependent measurements and different SOH will be presented in the future.

Figure 11. a shows the heatmap of the DRTs and (b) the associated DRTs as calculated and described in Section 4 as a function of SOC in 2.5% steps in discharge (left) and charge direction (right). As can easily be seen from this figure, 3 peaks, of which 1 does show a subpeak, are present although at different intensities over the complete SOC spectrum. For ease of discussion, these will be described as P1, P2A, P2B, P3 (right to left) and are labelled accordingly in the figure.

For heatmap visualisation, enhancing and visualising the lower peaks with small absolute values, the power-law transformation[24] as described by Eq. 24 is applied to the DRT values. The plotted values were smoothed with the MATLAB-Filter *imgaussfilt* and a sigma-

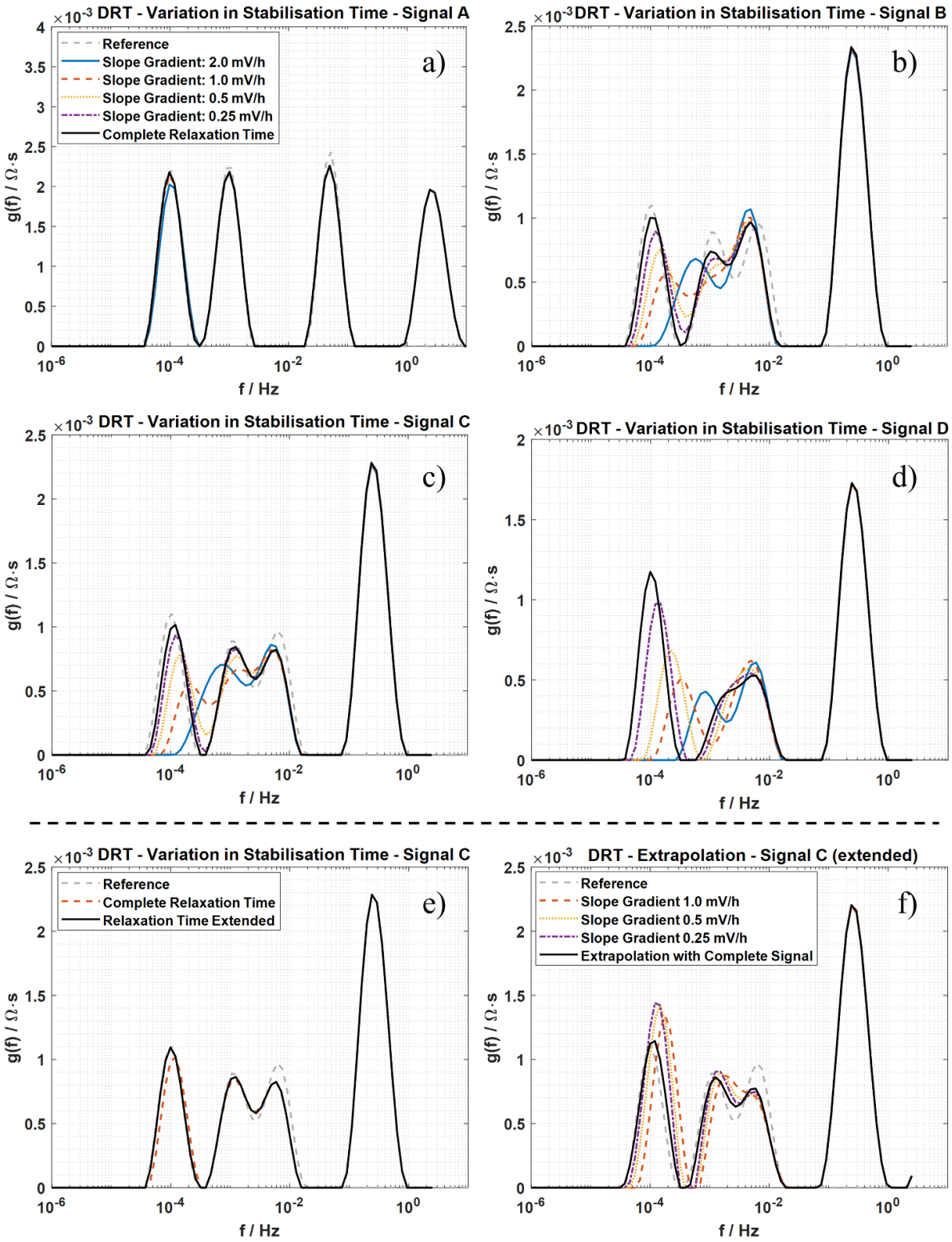

Figure 10. Comparison of changes in the DRT characteristic caused by different stabilization times for the pulse signals (the numeration correlates to the numberation of Table I. Slope gradients for the cut of the stabilization times are: 2.00 mV h^{-1}, 1.00 mV h^{-1}, 0.50 mV h^{-1} and 0.25 mV h^{-1}. In subfigure e an adaptation of test Signal C is performed by expansion of the stabilization time. The DRT calculations are similar. In f, the decribed method is used to extrapolate the DRT by termantion of the used signal at different slope gradients.

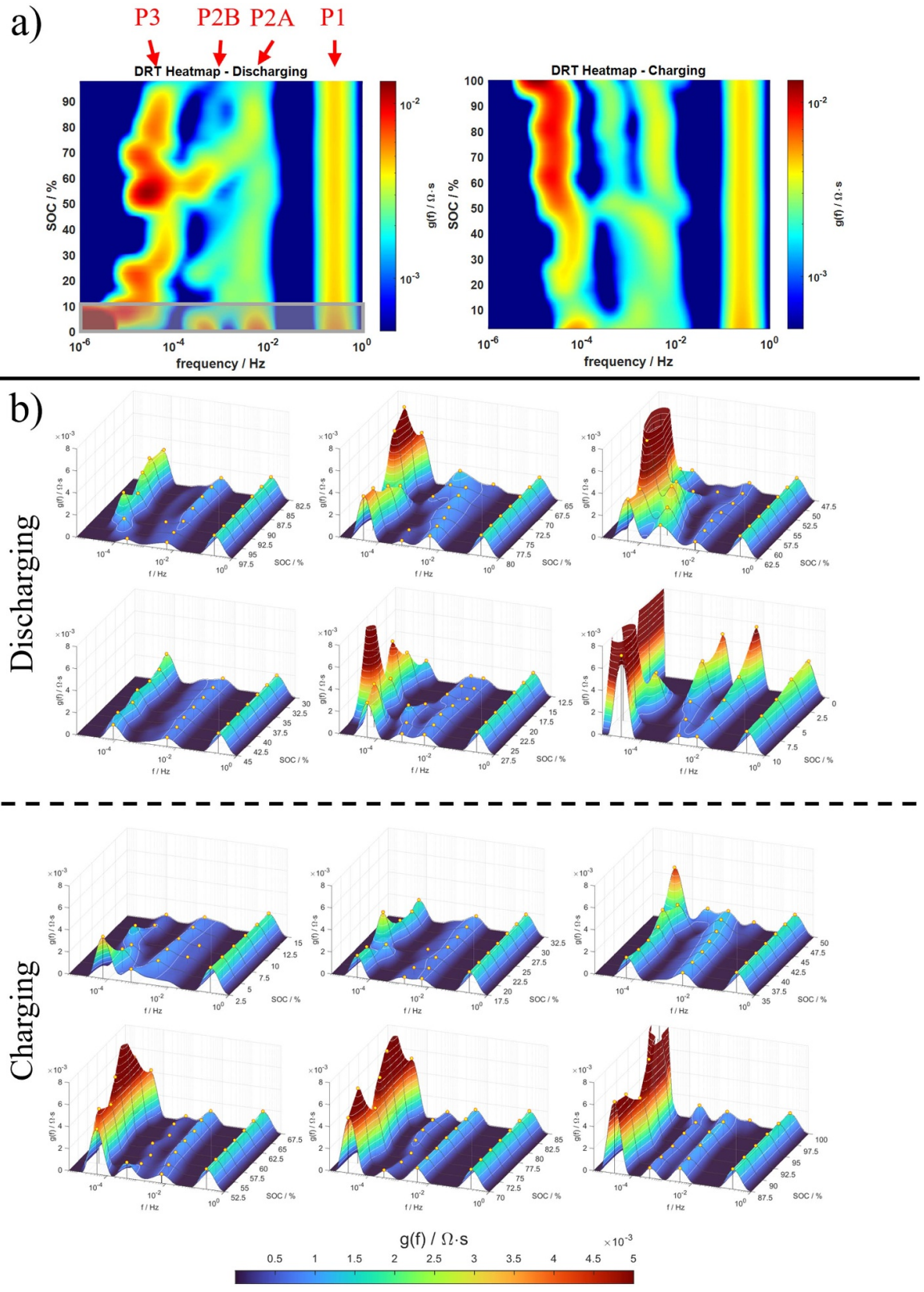

Figure 11. (a): Heatmaps of the analysis for discharging (97.5% to 0% SOC) and charging (2.5% to 100% SOC). Masked part shows a boundary value problem in the impedance calculation. (b): associated DRT plots.

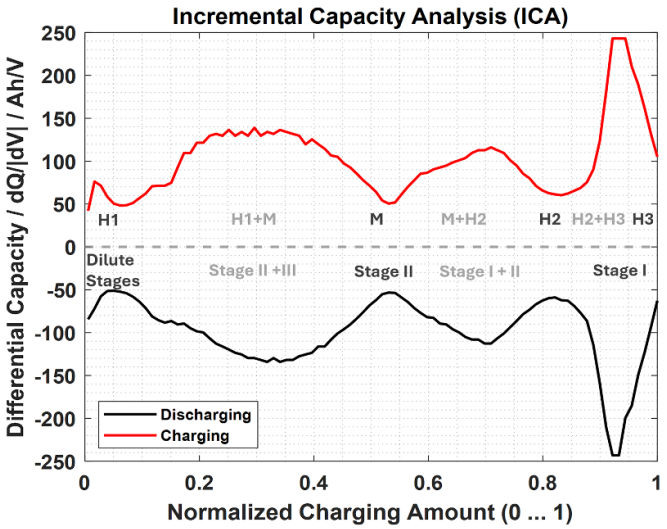

Figure 12. ICA of full cell measurements and for charging (positive) and discharging (negative). Differential stage levels of anode and cathode at their assumed positions are marked.

value of 1.2. The color bar is scaled with reference to $DRT_{\text{ref, min}} = 0$ and $DRT_{\text{ref, max}} = 1.4 \cdot 10^{-2}$ (the highest peak value: P3 at 50% SOC in discharge direction). An experimental γ-value of 1.8 is utilized.

$$DRT_{\text{Norm, absolut}} = \frac{DRT_{\text{smooth}} - DRT_{\text{ref, min}}}{DRT_{\text{ref, max}} - DRT_{\text{ref, min}}}$$

$$DRT_{\text{plot}} = \left(DRT_{\text{Norm, absolut}}\right)^{\frac{1}{\gamma}} \cdot \left(DRT_{\text{ref, max}} - DRT_{\text{ref, min}}\right) + DRT_{\text{ref, min}}. \quad [24]$$

To support the assignment of these DRT features to electrochemical processes, the DRT results are compared with the incremental capacity analysis (ICA) obtained from low-rate cycling (I=C/50) employing the same cell and shown in Fig. 12. The ICA provides an independent indication of SOC regions associated with phase transitions and therefore serves as an additional reference for the interpretation of the SOC-dependent DRT features in Fig. 11. As these measurements were performed on a complete cell, the summation of the anode and cathode effects on full cell level is visible, which results in overlap of the peaks related to the anode and cathode phase transitions. Added text boxes highlight the different inflection points (hence maximum of each separate peak) and denote the resp. phase transition at each point.

With reference to Fig. 11, the first peak (**P1**) is centred around 0.25 Hz with a nearly constant DRT height. This peak is most likely due to electrolyte conductivity and all other (SOC independent as well as SOC dependent) fast processes.[25] A further determination of the processes requires a significantly higher sampling frequency (at least 3 orders of magnitude) to be able to discriminate the time constants for these processes. Still, even then, a complete picture of the fast processes would not be possible as inductive effects cannot be modelled by the DRT and hence are not visible in the presented methodology. As is well known from EIS measurements these are present in large scale automotive cells,[8] making EIS indeed the better option for higher frequencies. For these reasons, a deeper interpretation of P1 in the context of this paper is omitted.

The second and third peaks clearly show different behavior compared with P1. They are far less constant over the SOC range both in magnitude as well as in their location. Also, for P2 a difference between the location of the splitting in 2 subpeaks (**P2A** & **P2B**) between the discharging and charging is observable. These peaks are attributed to slow Li-diffusion inside the electrodes. Schönleber[26] being one of the very few to perform measurements on these low frequencies, though on a different chemistry, came to the same conclusion. In his work the splitting of the P2 peak was, however, not observed and he did not address which of the peaks was due to anode and which to cathode diffusion.

Considering that the diffusion of the Li into the graphite (charge) resp. out of the graphite (discharge) involves a diffusion in a planar field with opening of low energy van der Waals forces for the interplanar structure, whereas in the cathode far higher ionisation energies of the transition metal ions have to be overcome during Li diffusion, P2 is attributed to the anode whereas P3 has been associated with the cathode.

As for an explanation of the splitting of peak 2 into 2 subpeaks, it is worthwhile to note that the first measurement occurred as a discharge. Now having a closer look onto the Li graphite phase diagram (Li_xC_6).[27] for $x = 1$ (fully charged) all interplanar sites are fully occupied (LiC_6, Stage I). On discharge, at first the Li^+-Ions will be removed randomly; however, a complete randomly distributed Li distribution is far from the energetic most preferable state. Instead, down to $x = 0.5$ a mixture of LiC_6 and LiC_{12} (Stage II) is present. While at first it is likely that a random extraction will occur but going further down to $x = 0.5$ (roughly 50% SOC)[b] a phase transition, involving inner particle diffusion of Li^+-ions, will occur. This needed inner particle diffusion will take its time and as such explains the gradual grow of peak 2B up to SOC 50%. It also explains the significant increase in time needed to reach the steady voltage (see Fig. 4. Continuing further down, the next stable phase exists at $x = 0.33$ (LiC_{18}, stage III). Also, here a certain, although less, amount of restructuring of the Li-ions inside the anode is needed, reflecting the local maximum for peak 2B at around SOC = 30%. Although there exists further evidence of a LiC_{24} phase it is generally assumed that downstream of Stage III a multitude of phases exists as the changes in the entropy are not extreme at these low doping levels (dilute states).[28]

The comparison of Figs. 11 and 12, reveals that the SOC regions in which pronounced changes in the DRT occur coincide with characteristic features in the ICA curves. In particular, the SOC-dependent splitting and variation of P2A and P2B occur in the same SOC range in which the ICA indicates graphite staging transitions. This supports the assignment of P2 to anode-related diffusion and phase-reorganisation processes. A more detailed analysis of this will be published in a future paper.

For small SOC values, the boundary problem is highlighted in Fig. 11a. Here, the time constants change rapidly within these pulse-specific SOC change whereby a calculation error results.

Now for the difference between charging and discharging, one should bear in mind that Fig. 11a right, from a physical point of view, has to be read bottom to top contrary to the left figure. Of course, the same phases as mentioned above, including the phase changes are occurring here.[15] However, there is a significant difference. While on discharge, one is emptying a stable system creating a metastable system; on charging, a stable system is slowly filled. Hence a stable phase (e.g. LiC_{12}) is slowly formed. Once the phase is fully built, the next Li just being inserted into the empty planes without the need for a significant restructuring of the phases. This to our opinion also explains the faster charging stabilization times compared to the same SOC-point discharging times.

NCA is also known to show different crystal structures depending on its lithiation degree as published by Nuroldayeva et al.[29] Given that these changes are primarily due to higher order-disorder phase transitions, the differences are far less pronounced as for the Li_xC_6 anode and primarily due to differences in the oxidation state of the different transition metals. These result in several long range Li-vacancy ordering (going from the R3m H1-state for the fully lithiated state to the monoclinic (M), H2, and H3 hexagonal phases

[b] As automotive Li-Ion batteries, for reasons of lifetime, are typically produced with a surplus of anode material, x does not correlate 1:1 with the SOC.

on maximum of the delithiation).[29,30] for the structurally comparable oxygen conducting perovskite materials, it is well known that such an ordering of the oxygen vacancies has a significant influence on the ionic conductivity.[31] Again, starting with the discharging, a start with the highly ordered H3 followed by a phase change of H3 → H2 around 90% SOC is to be expected. The entropy measurements of Nuroldayeva et al.[29] show a significant anomaly in this range, suggesting a relevant change in structure and hence also the conductivity. This correlates relatively well with the first peak observed around 80% SOC. It should be noted here that the cathode employed in this study has a slightly different Mn/Al-ratio as the mentioned study highly likely also changing the exact location of the H3→H2-transition. Further discharge brings the next high entropy change transition H2→M. This one being around 55% also somewhat lower as reported by Nuroldayeva et al.[29] The final transition M → H1 occurring around 25% in our case.

Now going again with the charging, the cathode is slowly stripped of the Li. This is highly likely associated with the afore mentioned slow disorder-order transitions and therefore there are less pronounced peaks (otherwise expressed, despite the really low stabilization limit of 0.2 mV h^{-1} for the pulse measurements, the measurements might not have been in phase stability on the cathode, which explains the relative straight yet high peaks at SOC >50%). A similar effect has been reported for the oxygen conductivity in the structurally close perovskites,[32] where stabilization times of up to 700 h were recorded, depending on the Sr doping level in $La_{1-x}Sr_xCoO_{3-\delta}$, where this doping level directly correlates with the oxygen vacancy amount and thus ordering).

Conclusions

A pulse-fitting method was applied/modified/developed to determine the impedance characteristics and dominant time constants of lithium-ion batteries. The DRT is calculated based on the time-dependent overpotential response to current pulses. The primary focus of this work was the systematic extension of the classical approach based on short charge/discharge pulses to ensure robustness and applicability under realistic automotive boundary conditions (large SOC changes).

To this end, the original formulation was modified by substitution of the analytical solution with a numerical convolution framework, enabling the treatment of non-ideal current profiles. The incorporation of a dynamic OCV description allowed the methodology to account for SOC variations during the pulse, thereby mitigating boundary value artefacts and extending the validity of the approach to longer excitation signals technically relevant current levels. In addition, Tikhonov regularisation was introduced to stabilize the solution in the presence of measurement noise, while diagonal weighting and column scaling ensured invariance of the results with respect to sampling frequency and improved numerical conditioning.

Beyond these methodological improvements, the solver formulation itself was adapted by introducing a quadratic programming approach. This resulted in enhanced stability and robustness, particularly for ill-conditioned problems and extrapolated frequency ranges. To further address practical limitations associated with short stabilization times, a dedicated extrapolation strategy for the DRT representation has been developed, enabling a more reliable estimation of long time-constant processes.

The applicability of the optimized method was demonstrated using both synthetic and experimentally obtained pulse signals, including standard OCV measurement data. The results show that the approach enables the extraction of low-frequency impedance information and diffusion-related time constants without requiring dedicated impedance spectroscopy measurements at low frequencies. This provides detailed insight into internal electrochemical processes across the SOC range, even for large-format automotive cells and under constrained measurement conditions. The method was shown to allow for the detection of phase transitions occurring on the anode and cathode.

It should be noted that the present work does not yet constitute a validation under arbitrary in-vehicle operating conditions. The investigated signals represent automotive-relevant but controlled pulse measurements. Application to actual vehicle operation, where excitation currents may be highly dynamic and superimposed by inverter-induced ripple or other drivetrain-related disturbances, requires further investigation.

Overall, the presented methodology offers a robust and flexible framework for time-domain impedance analysis, bridging the gap between laboratory-grade characterization methods and real-world battery operation. The ability to derive high-fidelity information on diffusion processes and system dynamics from standard test procedures makes it a valuable tool for advanced state estimation, model development, and future in-vehicle diagnostics.

Acknowledgments

The authors would like to thank the employees of AUDI AG and KIT for the constructive discussions during the preparation of this paper.

Credit author statement

Rico Klink: Conceptualization, Data curation, Formel analysis, Visualization, Writing—Original draft. **René H. E. van Doorn:** Supervision, Writing—review & editing. **André Weber:** Supervision, Writing—review & editing.

ORCID

Rico Klink https://orcid.org/0009-0003-8984-0304
René H. E. van Doorn https://orcid.org/0009-0007-8154-5684
André Weber https://orcid.org/0000-0003-1744-3732

References

1. S. Peng, Q. Ling, M. Yang, C. Bao, X. Zhong and P. Wang, "A high-precision and fast measurement method for li-ion battery EIS." *IEEE Trans. Instrum. Meas.*, **74**, 1–13 (2025).
2. M. Oldenburger, B. Bedürftig, A. Gruhle, F. Grimsmann, E. Richter, R. Findeisen and A. Hintennach, "Investigation of the low frequency Warburg impedance of Li-ion cells by frequency domain measurements." *J. Energy Storage*, **21**, 272 (2019).
3. D. Klotz, M. Schönleber, J. P. Schmidt and E. Ivers-Tiffée, "New approach for the calculation of impedance spectra out of time domain data." *Electrochim. Acta*, **56**, 8763 (2011).
4. M. A. Cabanero, N. Boaretto, M. Röder, J. Müller, J. Kallo and A. Latz, "Direct determination of diffusion coefficients in commercial li-ion batteries." *J. Electrochem. Soc.*, **165**, A847 (2018).
5. K. Fröhlich, I. Abrahams and M. Jahn, "Determining phase transitions of layered oxides via electrochemical and crystallographic analysis." *Sci. Technol. Adv. Mater.*, **21**, 653 (2020).
6. C. J. Wen, B. A. Boukamp, R. A. Huggins and W. Weppner, "Thermodynamic and mass transport properties of "LiAl"." *J. Electrochem. Soc.*, **126**, 2258 (1979).
7. J. H. Park, H. Yoon, Y. Cho and C. Y. Yoo, "Investigation of lithium ion diffusion of graphite anode by the galvanostatic intermittent titration technique." *Materials*, **14**, 4683 (2021).
8. R. Klink, R. H. E. van Doorn and A. Weber, "Review—electrochemical impedance spectroscopy for lithium- ion batteries: measurement and analysis (for automotive applications)." *Curr. Opin. Electrochem.*, **54**, 101768 (2025).
9. E. Goldammer and J. Kowal, "Determination of the distribution of relaxation times by means of pulse evaluation for offline and online diagnosis of lithium-ion batteries." *Batteries*, **7**, 36 (2021).
10. J. P. Schmidt and E. Ivers-tiffée, "Pulse-fitting—A novel method for the evaluation of pulse measurements, demonstrated for the low frequency behavior of lithium-ion cells." *J. Power Sources*, **315**, 316 (2016).
11. C. E. Shannon, "Communication in the presence of noise." *Proc. IRE*, **37**, 10 (1949).
12. J. Yin, C. Drießen, R. Klink, S. Kizio, J. Moser, C. Ellersdorfer and P. Höschele, "Implementation of gas formation into a finite-element model for the mechanical swelling simulation of lithium-ion batteries." *J. Energy Storage*, **150**, 120376 (2026).
13. M. Petzl and M. A. Danzer, "Advancements in OCV measurement and analysis for lithium-ion batteries." *IEEE Trans. Energy Convers.*, **28**, 675 (2013).
14. M. D. Levi and D. Aurbach, "Diffusion coefficients of lithium ions during intercalation into graphite derived from the simultaneous measurements and modeling of

electrochemical impedance and potentiostatic intermittent titration characteristics of thin graphite electrodes." *J. Phys. Chem. B*, **101**, 4641 (1997).
15. M. Heß and P. Novák, "Shrinking annuli mechanism and stage-dependent rate capability of thin-layer graphite electrodes for lithium-ion batteries." *Electrochim. Acta*, **106**, 149 (2013).
16. C. Didier, W. K. Pang, Z. Guo, S. Schmid and V. K. Peterson, "Phase evolution and intermittent disorder in electrochemically lithiated graphite determined using in operando neutron diffraction." *Chem. Mater.*, **32**, 2518 (2020).
17. G. H. Golub, P. C. Hansen and D. P. O'leary, "Tikhonov regularization and total least squares." *SIAM J. Matrix Anal. Appl.*, **21**, 185 (1999).
18. J. Weese, "A reliable and fast method for the solution of Fredhol integral equations of the first kind based on Tikhonov regularization." *Comput. Phys. Commun.*, **69**, 99 (1992).
19. A. L. Gavrilyuk, D. A. Osinkin and D. I. Bronin, "The use of Tikhonov regularization method for calculating the distribution function of relaxation times in impedance spectroscopy." *Russ. J. Electrochem.*, **53**, 575 (2017).
20. B. Garda and Z. Galias, "Tikhonov regularization and constrained quadratic programming for magnetic coil design problems." *Int. J. Appl. Math. Comput. Sci.*, **24**, 249 (2014).
21. H. Dym, *Linear Algebra in Action*, Positive definite and semidefinite matrices, 2nd ed., vol. 78, (American Mathematical Society), pp. 171–83 (2013).
22. N. I. Gould, D. Orban, A. Sartenaer and P. L. Toint, "Superlinear convergence of primal-dual interior point algorithms for nonlinear programming." *Soc. Ind. Appl. Math.*, **11**, 974 (2001).
23. P. A. Absil and A. L. Tits, "Newton-KKT interior-point methods for indefinite quadratic programming." *Comput. Optim. Appl.*, **36**, 5 (2007).
24. L. Pérez-enriquez, M. Jiménez-domínguez, N. García-rojas, S. Zapotecas-martínez and L. Altamirano-robles, "Image contrast enhancement: the synergistic power of a dual-gamma correction function and evolutionary algorithms." *Computa.y Sistem.*, **29**, 91–101 (2025).
25. B. Bera, A. Roy, P. Young, D. S. Aaron and M. M. Mench, "A formal analysis of internal resistances of li-ion cells using EIS and DRT to simultaneously probe both working electrodes." *Adv. Mater. Technol.*, **11**, 1–15 (2026).
26. M. Schönleber, "Verfahren zur charakterisierung des niederfrequenzverhaltens von lithium-ionen batterien" *PhD Thesis* Karlsruher Institut für Technologie (KIT) (2017).
27. M. Winter and J. O. Besenhard, "Electrochemical lithiation of tin and tin-based intermetallics and composites." *Electrochim. Acta*, **45**, 31 (1999).
28. Q. Liu, S. Li, S. Wang, X. Zhang, S. Zhou, Y. Bai, J. Zheng and X. Lu, "Kinetically determined phase transition from stage II (LiC(12)) to Stage I (LiC(6)) in a graphite anode for li-ion batteries." *J. Phys. Chem. Lett.*, **9**, 5567 (2018).
29. G. Nuroldayeva, D. Adair, Z. Bakenov and B. Uzakbaiuly, "Revealing phase transition in ni-rich cathodes via a nondestructive entropymetry method." *ACS Omega*, **8**, 37899 (2023).
30. C. Xu, P. J. Reeves, Q. Jacquet and C. P. Grey, "Phase behavior during electrochemical cycling of ni-rich cathode materials for li-ion batteries." *Adv. Energy Mater.*, **11** 2003404 (2020).
31. H. Kruidhof, H. J. M. Bouwmeester, R. H. E. V. Doorn and A. J. Burggraaf, "Influence of order-disorder transitions on oxygen permeability through selected nonstoichiometric perovskite-type oxides." *Solid State Ion.*, **63–65**, 816 (1993).
32. R. H. E. van Doorn and A. J. Burggraaf, "Structural aspects of the ionic conductivity of La1−xSrxCoO3−δ." *Solid State Ion.*, **128**, 65 (2000).